NeuroImage 54 (2011) S165–S175

Contents lists available at ScienceDirect

NeuroImage

journal homepage: www.elsevier.com/locate/ynimg

Evaluation of fiber bundles across subjects through brain mapping and registration of diffusion tensor data

Darshan Pai [a], Hamid Soltanian-Zadeh [b,c,*], Jing Hua [a]

[a] Department of Computer Science, Wayne State University, Detroit, MI, USA
[b] Image Analysis Laboratory, Radiology Department, Henry Ford Health System, Detroit, MI, USA
[c] Control and Intelligent Processing Center of Excellence (CIPCE), School of Electrical and Computer Engineering, University of Tehran, Tehran, Iran

ARTICLE INFO

Article history:
Received 5 December 2009
Revised 6 May 2010
Accepted 29 May 2010
Available online 12 June 2010

Keywords:
Analysis of fiber bundles
Diffusion imaging
Epilepsy
Shape analysis
Multimodality fusion
Medical image processing

ABSTRACT

This paper presents a visualization and analysis framework for evaluating changes in structural organization of fiber bundles in human brain white matter. Statistical analysis of fiber bundle organization is conducted using an anisotropy measure, volume ratio (VR), which is ratio of anisotropic and isotropic components. Initially fiber bundles are tracked using a probabilistic algorithm starting from seed voxels. To ensure accurate selection of seed voxels and to prevent operator bias, a reference brain (MNI_152) is used when marking ROIs. Individual structural MRI brain scans are mapped to the reference using volumetric conformal parameterization. This mapping preserves topology and aligns features perfectly making it a robust and accurate registration technique. One-to-one mapping to the template allows ROI selection and subsequent transfer of ROI to structural MRI of subject. Affine registration coregisters structural MRI and DTI. Seed voxels are mapped to DTI using the resulting transformation parameters. To evaluate the proposed approach, MRI and DTI of 12 normal volunteers and 15 medial temporal lobe epilepsy patients are used. First, a statistical hypothesis testing is conducted to test for anisotropy changes in cingulum and fornix fiber bundles of epileptic patients. Experimental results reveal a 40% decrease in anisotropy levels of cingulum in patients compared to volunteers. They also show a 25% overall decrease in anisotropy of fornix. Secondly, shapes of the bundles are visualized in 3D illustrating that the bundles of epileptic patients are bumpy while those of normal volunteers are smooth.

Introduction

The advent of high-end and computationally intensive machines has improved the acquisition of various 3-D neuroimaging data. The complexity, scale, and resolution of the images have increased significantly in recent years. As a result, huge amount of data is available for analysis. Different imaging modalities provide complementary information regarding the anatomy, physiology, and structure of the living organs and tissues. They include anatomical and diffusion data provided by magnetic resonance imaging (MRI) and diffusion tensor imaging (DTI); molecular imaging and functional data provided by positron emission tomography (PET) and functional MRI (fMRI); and electrophysiological data provided by electroencephalography (EEG). Normal brain function is characterized by various interactions between specific regions of the brain. A framework combining the various facets of the anatomy and physiology of the human brain is a requirement for a robust pathological analysis. We present a framework for evaluation of the fiber bundles based on two modalities, MRI and DTI, which together provide an excellent representation of the white matter organization as well as changes associated with disease.

Statistical analysis (Miller et al., 1997; Styner et al., 2003; Thompson and Toga, 2002) in brain abnormality studies are typically population-based comparisons that reveal significant differences between healthy volunteers and patients. The results can help achieve important objectives in many neuroscience studies, for instance, delineating the anatomical region affected by disease facilitates future course of treatment and surgical planning. Given the complex anatomy of the brain, a robust registration strategy is required for accurate alignment of inter-subject brain images. An accurate depiction of normal anatomical variability in specific regions across subjects depends on the homology between them. In recent years, various brain mapping algorithms have been developed (Miller et al., 1997; Styner and Gerig, 2001; Thompson et al., 2001) to address this dependency and to allow an accurate statistical analysis. Mapping algorithms can be classified into two categories: implicit image intensity-based technique; and explicit computational geometry-based technique. The intensity-based technique does not require segmentation of the brain structures (regions). It uses an implicit characterization based on intensity distributions. This facilitates

* Corresponding author. Radiology Image Analysis Lab., Henry Ford Health System, One Ford Place, 2F, Detroit, MI 48202, USA. Fax: +1 313 874 4494.
E-mail address: hamids@rad.hfh.edu (H. Soltanian-Zadeh).

1053-8119/$ – see front matter © 2010 Elsevier Inc. All rights reserved.
doi:10.1016/j.neuroimage.2010.05.085

voxel-based analysis and not a surface-based analysis (Muzik et al., 2007; Friston et al., 1994; Muzik et al., 2000). The geometry-based technique takes advantage of additional explicit geometric properties of the brain structures and achieves accurate mapping and registration of the brain images permitting surface-based analysis. Freesurfer (Fischl et al., 1999) and Caret (Essen et al., 2001) are popular methods that combine the geometry with automatic anatomical labeling methods to achieve a powerful representation for analyzing cortical brain structures. Since geometry is an important aspect, preprocessing is a required first step. Various representations have been proposed for surface analysis. They include curvature-based representations (Vemuri et al., 1986), regional point representations (Chua and Jarvis, 1997), spherical harmonics (Kazhdan et al., 2003), shape distributions (Osada et al., 2002), spline representations (Camion and Younes, 2001), and harmonic shape images (Zhang, 1999). These methods, however, suffer from mismatches due to insufficient discriminative power. Riemannian geometry has a distinct advantage since it is based on intrinsic geometric properties of the manifold and corrects for this mismatch (Drury, 1999; Wang et al., 2005). Conformal mapping based on the harmonic energy minimization on a 2D manifold allows for accurate registration in genus zero surfaces, which is topologically equivalent to the cortical brain surface. This technique has been extended to 3D manifolds for volumetric mapping and analysis (Wang et al., 2004). Moreover, the mapping is bijective and is easily transferred to the native space of the subject. In this paper, we present a constrained conformal mapping approach for matching structural MRI images.

DTI is the preferred modality for visualizing the structural organization of the white matter microstructure. The anisotropic properties and directional diffusivity obtained from the DTI tensor at each voxel is used to analyze and detect white matter abnormalities. Statistical analysis and matching, however, is not straightforward in DTI mainly due to the orientation information inherent in the data. Spatial Normalization (Park et al., 2003; Jones et al., 2002) of the DTI brain dataset, for quantification of diffusion tensor differences between populations, were conducted with unsatisfactory results because only intensity was considered (Wakana et al., 2004). The Tract-Based Spatial Statistics (TBSS) method (Smith et al., 2006) improves on this by using skeletonization to normalize the fractional anisotropy (FA) images which measures the voxel-based statistics along major fiber tracts. In general, spatial normalization is non-trivial and can modify the real tensor orientation of the underlying data (Alexander et al., 2001). It can potentially modify abnormalities captured in the native space, for instance, structural changes in the fiber tracts.

The most popular method to identify changes in the structural organization of the white matter fibers is tractography, which is characterized as deterministic fiber tracking and probabilistic fiber tracking. Deterministic fiber tracking tracks single-fiber populations (Parker, 2000; Hagmann, 2004; Mori et al., 1999; Frank 2001) by following the direction of the major eigen-vector of the tensor ellipsoid at each voxel. Major eigen-vectors are well-defined at places where the anisotropy is high and the tracts are reliable only for linear anisotropy diffusion profiles. Probabilistic tracking improves on this disadvantage by introducing uncertainty in the tracking algorithm for estimating the fiber directions. Consequently, the algorithm allows tracking in hard to reach areas (Brehens et al., 2003; Friman et al., 2006). Since the tracks do not represent real fiber orientations because of the random sampling criteria, we rely on the connectivity strength prediction between voxels to describe a global probability connectivity map. Various methods for computing this connectivity employ techniques that achieve a greedy or global optimum and have been studied extensively.

In this paper, we concentrate on using anisotropy markers for measuring tract integrity. Our hypothesis testing studies rely on the volume ratio (VR) to characterize structural changes in white matter fiber bundles. This hypothesis is evaluated by measuring white matter differences in the fornix and the cingulum fiber bundles of medial temporal lobe epilepsy patients. MRI brain scans of individual subjects are parameterized onto a curvature-constant volume representing the canonical domain for mapping. Additionally, the anatomical and diffusion images of the same subject are registered using an affine registration algorithm. Since these mappings are bijective, the statistical results can be generated in the native space of the DTI image. The regions of interests (ROIs) that define the seed voxels for tracking are chosen on the template and transformed to the native DTI space of the subject using the transformation parameters obtained during registration. The final results show that anisotropy differences in the fiber bundles measured using the mean VR is significant between the patient and the normal groups. Moreover, we employ a region-growing algorithm to determine the shapes of these bundles providing a visual interface to identify shape changes associated with disease. The method and the results are explained in detail in the following sections.

Materials and methods

Subjects and imaging data

The MRI and DTI data of fifteen medial temporal lobe epilepsy patients (10 males, 5 females, ages 43 ± 16) and twelve normal volunteers (9 males, 3 females, ages 32 ± 5) enrolled in research studies approved by the IRB committee of Henry Ford Hospital, Detroit, Michigan, USA were used in this work. All imaging data were acquired on a 3 Tesla GE Signa system (General Electric, Milwaukee, WI, USA) at Henry Ford Hospital, Detroit, Michigan, USA. The imaging protocol included anatomical T1-weighted images and diffusion tensor images. The T1-weighted images were acquired in the coronal plane using a 3D inversion recovery (IR) spoiled gradient-echo (SPGR) sequence with TR/TI/TE = 7.6/1.7/500 ms, flip angle = 20°, field of view (FOV) = 200 mm × 200 mm, matrix size = 256 × 256, pixel size = 0.781 mm × 0.781 mm, and slice thickness = 2.0 mm. The DTI data were acquired in the axial plane using 25 non-collinear weighting directions and a single shot echo planar imaging (EPI) sequence with a b-value of 1000 s/mm^2. Each volume covered a 240 mm × 240 mm field of view with 0.9375 mm × 0.9375 mm in-plane resolution and 2.6 mm slice thickness with no inter-slice gap.

Conformal mapping

Conformal parameterization of the 3D-representative geometry in the 2D space is a preferable choice since it simplifies computational complexity. Gu et al. (2004) described a harmonic energy minimization algorithm for generating a conformal map between genus zero surfaces and a canonical surface (sphere). The canonical domain is curvature-constant, which eliminates problems associated with distance fields in the Euclidian space. Moreover, matching cortical patterns in the canonical domain becomes highly efficient.

We represent our standardized space as canonical domain structures of closed genus zero topology and term it as the Conformal Brain Model (CBM). A genus zero topology is a geometric structure with no holes. For statistical analysis, a representative brain is needed which will be the template for matching. This model can be one of the datasets used for analysis or an average brain representation from a training set of normal subject brains. We chose the MNI_152 atlas brain as our reference template for analysis and the corresponding map will be the template CBM. The following paragraph explains the method to compute the template CBM.

Initially, we concentrate on the conformal mapping of the brain cortical surface. The brain cortical surface can be viewed as a closed genus zero surface that can be parameterized in the spherical domain. The mapping is defined using the function $f: S^2 \rightarrow R^3$, where f is a vector

valued function that maps the coordinates of the sphere in spherical coordinates onto the cortical brain surface. Fig. 1 provides a good illustration for the conformal mapping. Consider two surfaces M and N with a conformal mapping ϕ between them. If $\gamma_1$and γ_2 are two curves defined on M with an intersecting angle α, then the corresponding curves $\phi(\gamma_1)$ and $\phi(\gamma_2)$ defined on N will intersect at the same angle α. This is demonstrated by the checkerboard pattern on the surfaces shown in Fig. 1 illustrating that the angles are preserved. For the function $f{:}M{\rightarrow}N$ defined above, the mapping can be made conformal by minimizing the harmonic energy of the map (Gu et al., 2004). Genus zero surfaces are defined by meshes. For a simplicial complex $|K|$, and the map f, the implicit energy is defined by

$$E = \sum_{u,v\in k} k_{u,v}\|f(u)-f(v)\|^2, \tag{1}$$

where u and v denote vertices, $\{u,v\}$ denotes the edge linking u and v, and $k_{u,v}$ is a constant representing the string energy between u and v. Since f represents a vector valued function, $\vec{f} = \{f_0, f_1, f_2\}$, defined over $|K|$, the energy of f is computed by

$$E\left(\vec{f}\right) = \sum_{i=0}^{2} E(f_i). \tag{2}$$

The function f is harmonic if and only if the Laplacian of f in the tangential direction is zero. This can be easily solved using the steepest descent algorithm of the form

$$\frac{d\vec{f}(t)}{dt} = -\Delta\vec{f}(t), \tag{3}$$

such that the string energy is minimized. This map is conformal and represents a smooth and angle-preserving mapping from a genus zero surface M, representing the brain surface, to a unit canonical sphere S^2. The conformal factor $e^{2\lambda}$ and the mean curvature on the surface h are treated as functions on the sphere. These functions completely define the surface S^2 uniquely except for a rigid rotation (Gu et al., 2004). A Cartesian coordinate system is defined which specifies a 3D rotation transformation to guarantee a unique orientation of the sphere (Zou et al., 2006). Note that this mapping is only a partial step for creating the template CBM.

Volumetric conformal mapping

In the volumetric case, the brain volume is represented by the tetrahedral mesh. We keep the same genus zero requirements that will now map the tetrahedral mesh to a solid ball. The tetrahedral mesh of a brain is shown in Fig. 2a. Fig. 2b shows the left-hemisphere highlighting the internal structures. The procedure to create the template CBM is exactly the same as before. The surface map is fixed and the algorithm proceeds to minimize the harmonic energy of the internal structures. This step is computationally intensive because of the increased resolution. The algorithm computes the template CBM as shown in Fig. 2d. The template CBM represents the canonical space for brain mapping. The volumetric conformal map also preserves the geometry between the two volumes. A textured slice shown in the cut section of the sphere (Figs. 2e–f) highlights the fact that the geometry is preserved during mapping.

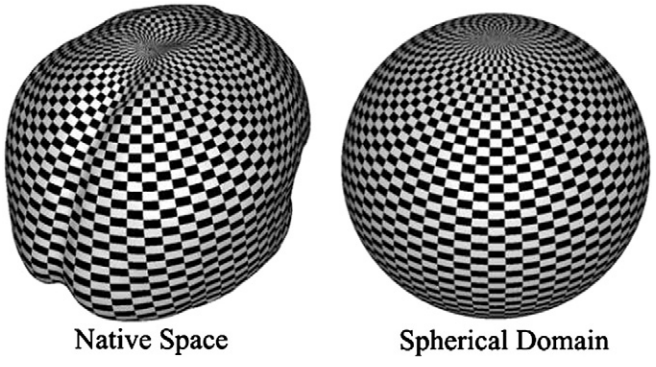

Fig. 1. An illustration of conformal mapping where the angles of the squares in the checkerboard pattern are preserved.

Brain volume matching using CBM-landmark-constrained shape optimization

The CBM provides a 3D-representation of the brain volume geometry in the canonical domain. For cross-subject analysis, the CBM should be homologous across all datasets. This cannot be achieved with conformal mapping alone and alignment between its various anatomical features is important. Features are sulcal landmarks and internal subcortical structures most common across brain populations. These include cortical patterns, such as the ones shown in Figs. 3c and 4a and internal brain structures (Fig. 3a) like the corpus callosum, pons, anterior commissure, and cingulate. Structural MRI effectively delineates these features and is the preferred modality for alignment. An expert neuroanatomist selects the features for all the individual MRI scans under study. A well-balanced set of features across the brain guarantees the accuracy of the alignment. Some of the surface landmarks shown in Fig. 4 are central sulcus, pre-central sulcus, post-central sulcus, superior frontal sulcus, sylvian fissure, superior temporal sulcus, inferior temporal sulcus, parieto-occipital, and transverse occipital sulcus. Internal landmarks are edges and points, the AC–PC line, and edges of well-known structures internal to the brain. The landmarks are chosen as a set of ordered point's $\{P_i\}$ across the brain volume. Conformal mapping to the template CBM orients the brain volumes while the landmark constraints minimize the inherent variability in the anatomical domain and matches two CBMs perfectly.

Various ideas has been proposed (Gu et al., 2004; Wang et al., 2005) tackling this issue. A landmark-constrained conformal mapping (Zou et al., 2006) is described below. Given a set of point's $\{P_i\}$ representing the landmarks, conformal mapping is employed on a template brain without any landmark constraints. The MNI_152 brain atlas, a standard averaged brain from a database of 152 normal subjects (Fig. 4a), is mapped to the spherical domain and the harmonic energy minimization on the surface and the subsequent minimization on the volume computes the conformal model termed the template CBM (Fig. 4b). Fig. 4 illustrates the steps of the matching process. Fig. 4b shows the template CBM with the landmarks $\{p_i \in C_1\}$ defined on it. For an individual subject, we assume initially that the landmarks are very close to the ones defined on the template $\{q_i \in C_2\}$. The initial mapping of the subject onto the sphere is shown in Fig. 4c. The set of ordered points is ensured to have the same cardinality. A landmark-constrained optimization is computed using the steepest descent algorithm as described in the previous section. This procedure still minimizes the harmonic energy but every ordered point $\{p_i\}$ is constrained to be aligned with its counterpart $\{q_i\}$ on the template. The next step is to align the brain regions between the landmarks. This is achieved by matching the anatomical shapes using a distance function in the shape space given as

$$d(S_1, S_2) = \int_v ((\lambda_1-\lambda_2)^2 + (h_1-h_2)^2)d\mu \tag{4}$$

where $S_1 = (\lambda_1, h_1)$ and $S_2 = (\lambda_2, h_2)$ and $d\mu$ is the volume element on the sphere. S_1 and S_2 are the two spherical volumes to be matched and λ and h are the conformal factor and the mean curvature, respectively defined as functions on the sphere that determine the spherical map

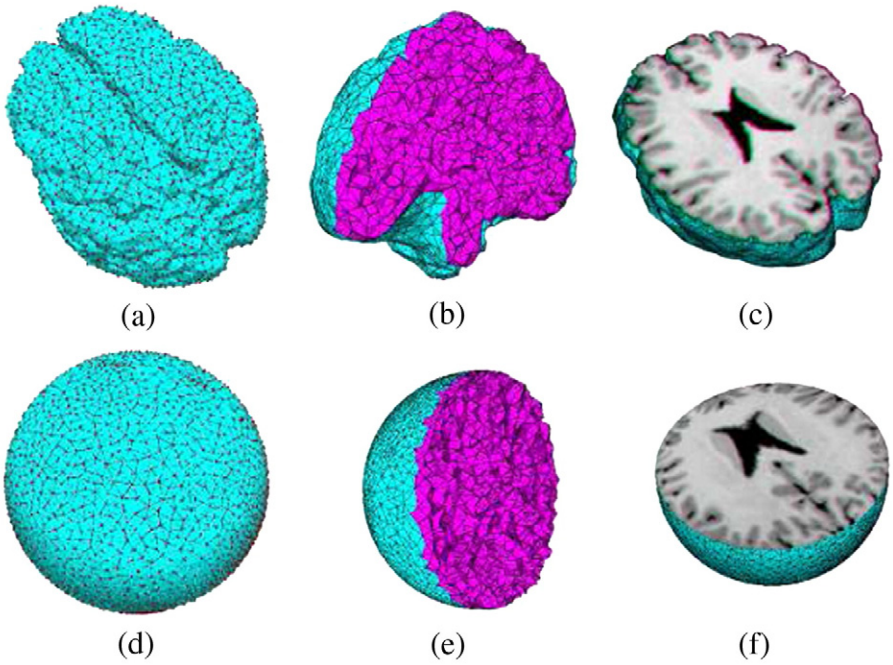

Fig. 2. An illustration of conformal mapping applied to brain: (a) tetrahedral mesh equivalent of the brain volume; (b) internal mesh structure; (d) the solid ball created by volumetric conformal mapping; (e) internal structure of the brain after the conformal mapping; (c), (f) interpolated slices which show that the conformal mapping preserves the brain geometry.

unique up to rigid motions in R^3. This optimization determines the optimal shape transformation functional that minimizes the distance field between the two shapes. To ensure that the optimization is stable and also to use well-known features that are stable across the datasets, very coarse smoothing is allowed on the brain surface. Fig. 4d shows the subject brain CBM aligned to the template CBM.

Affine registration

The conformal mapping is invertible and has a one-to-one mapping between individual MRIs and the template. The template will be used for choosing ROIs and other functional elements or areas. The ROIs for seeding the voxels for fiber tracking is chosen on the template. Through affine registration, the voxels are mapped onto the individual DTI scans for tracking. We argued before on the potential problems associated with spatial normalization of the DTI, which affects the tensor orientation. Hence, instead of warping the DTI to the MRI, the registration parameters are saved. We choose the non-diffusion weighted image, i.e., the image with no diffusion gradient ($b=0$), and register it to the MRI using 12-parameter affine registration. Combining the affine transformation parameters with the conformal map creates the transformation space necessary to convert the voxels selected on the template down to each individual DTI image. This is advantageous since the same ROIs are seeded across all the subjects preventing bias. The ROIs will represent the same spatial region across the subject populations. Affine image registration is available in the well-known packages like FSL (Brehens et al., 2003), AIR (Woods et al., 1998), and SPM.

Probabilistic fiber tracking

The final step is to generate quantitative measures for the statistical analysis study. For anisotropy analysis, we track the neural fibers from the DTI data. We briefly describe the underlying model of the diffusion tensor image. Diffusion MRI is a relatively new modality and relates displacements of water molecules, p, in the tissue with the image intensities. White matter tissue in the human brain contains bundles of neural fibers connecting various functional areas. For brain images, p, along these fiber directions is higher. Hence, the probability distribution of p represents a cigar shaped structure (Fig. 5c) indicating high anisotropy. Diffusion tensor MRI (DT-MRI) models p as a simple diffusion with a Gaussian profile given by

$$G(x;D,t) = ((4\pi t)^3 \det(D))^{-1/2} \exp\left(\frac{-x^T D^{-1} x}{4t}\right), \quad (5)$$

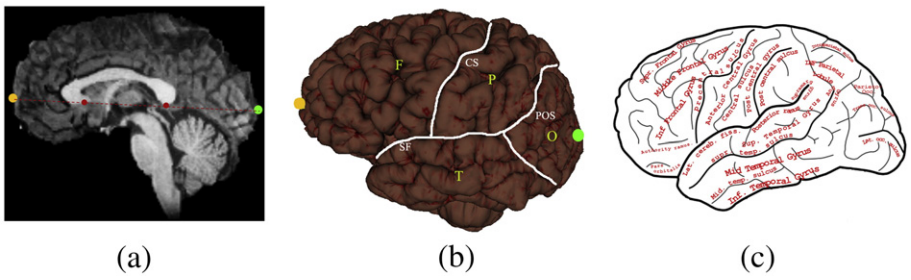

Fig. 3. A sagittal slice (a) and a surface view (b) of the brain that may be used to select the landmarks in comparison to an atlas (c) that shows various landmarks on the brain surface.

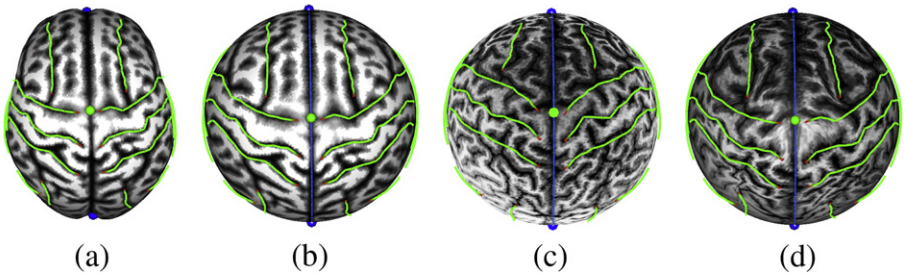

Fig. 4. The MNI 152 atlas (a) and the template CBM (b). Matching the features in (b) to a CBM of an individual (c) generates an optimized landmark-constrained version (d).

where D is the diffusion tensor and t is the diffusion time. The MRI acquisition sequences follow the Stejskal–Tanner imaging sequence (Stejskal and Tanner, 1965), which models the observed intensity of anisotropic samples as

$$S = S_0 e^{-bg^t Dg}, \tag{6}$$

where b defines a parameter of the sequence called the weighting factor. To sample the ellipsoid uniquely, the 3×3 diffusion tensor D needs to be solved. This requires at least six independent measurements along different gradient orientations g. The principal directions of the tensor at each voxel are calculated using singular value decomposition. The eigen-values specify an orientation-independent measure of the anisotropy at each voxel and the corresponding eigen-vectors specify the directions of water diffusion. Reconstructing the white matter pathways from principal directions provide a means for assessing pathological changes in the white matter. We describe two methods to track these pathways.

Deterministic tracking tracks fibers along the primary eigen-direction e_1 at each voxel. Many fiber bundles have been reliably tracked by this method and validated. The single direction criterion for tractography makes it difficult to track in areas where the diffusion is more isotropic, for instance, complex fiber neighborhoods ($\lambda_1 \approx \lambda_2 \gg \lambda_3$) that correspond to multi-fiber orientation within a voxel, resulting in unreliable tracking results (see Fig. 5). To overcome these limitations, a probabilistic tracking algorithm is devised. We follow the algorithm derived by Friman et al. (2006) in his paper. The algorithm is based on a Bayesian inference and estimation scheme. Uncertainties, due to noise or complex fiber architectures, are not disregarded but captured in the model itself in the form of the posterior distribution at each voxel. Given a source region A, the probability of connectivity between A and a target region B is given by

$$p(A\rightarrow B|D) = \sum_{n=1}^{\infty} \int_{\Omega_{AB}^n} p(n)p(v_{1:n}|D), \tag{7}$$

where $p(v_{1:n}|D)$ is the probability of the fiber path going from A to B given the diffusion data D and Ω_{AB}^n represents the sampling space of the connectivity between A and B of path length 1 through n. Since Eq. (7) is not analytically solvable, a rejection sampling strategy is employed. A large number of sampled fiber paths starting from the source region A are drawn at random and the probabilities of the paths between A and B are evaluated. Each random path is evaluated locally in steps up until the predetermined length n. The steps are assumed to be unit length vectors, with the condition that each step depends only on the previous step. Since these samples reflect the model of the actual fibers, the posterior distribution at each step is calculated based on the diffusion data D at that voxel. This distribution based on the Bayes theorem is written as

$$p(\hat{v}_i, \theta|\hat{v}_{i-1}, D) = \frac{p(D|\hat{v}_i, \theta)p(\hat{v}_i|\hat{v}_{i-1})p(\theta)}{p(D)}. \tag{8}$$

The first term in the numerator is the likelihood at the current step and uses a constrained model based on a Gaussian diffusion profile. $p(\hat{v}_i|\hat{v}_{i-1})$ is the prior to indicate the dependence of the current step on the previous step. This assumption works well in a complex fiber neighborhood because there will always be a preference on the previous step. The nuisance priors, $p(\theta)$, address the parameters of the Gaussian profile modeled as dirac priors. As explained by Friman et al. (2006), using dirac priors significantly saves computation time. Finally, $p(D)$ is a normalizing constant that gives the probability distribution at $\hat{v}_i$ distributed over a unit sphere as shown in Fig. 6a. To draw a random path, the sphere is discretized uniformly into a finite set of unit vectors indicating possible directions. The next step direction is picked at random and added to the path. The fiber paths represent the sampling space of the source region. The fiber paths are illustrated in Fig. 6b.

Shape analysis of fiber bundles

Anisotropic differences are indicative of the changes in the structural organization of the fiber bundle. Abnormalities associated with changes in anisotropy can be visually inferred from the fiber bundle shape. We can quantify the shape differences using well-known measures such as curvature. Many researchers have presented

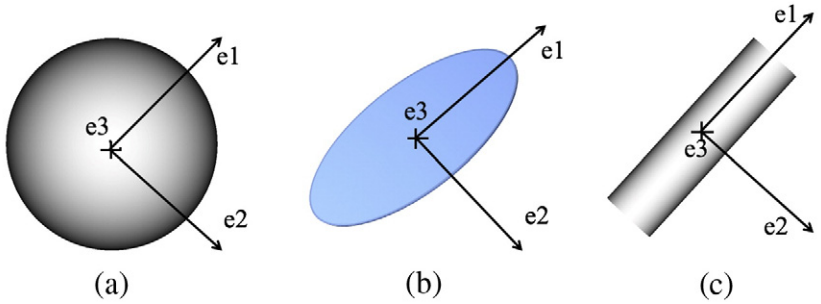

Fig. 5. (a) Isotropic profile ($\lambda_1 \approx \lambda_2 \approx \lambda_3$). (b) Ellipsoidal profile ($\lambda_1 > \lambda_2 \approx \lambda_3$). (c) Highly anisotropic cigar-shaped profile ($\lambda_1 \gg \lambda_2$ and $\lambda_1 \gg \lambda_3$). The eigen-vectors (directions) are shown in each case where e_1 is the primary eigen-direction.

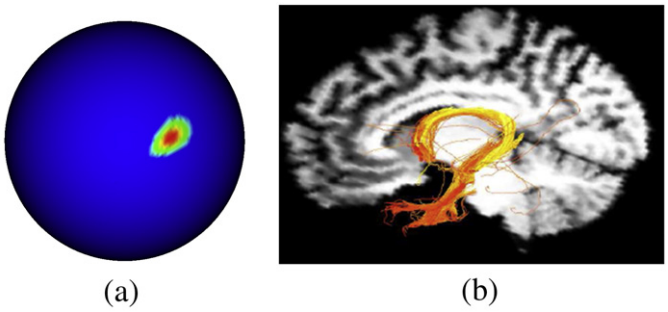

Fig. 6. (a) Posterior probabilities of voxels showing areas of high probability that can be used to identify most probable fiber path in each voxel. (b) Fornix bundle identified using probabilistic fiber tracking.

techniques to construct the fiber bundle surface. However, no specific analysis protocols are available that analyze the shape differences. Edge detection techniques (Schultz and Seidel, 2008; Kindlmann et al., 2007a) directly use important tensor components to calculate gradients, which represents the surface boundary of the fiber bundle. Melonakas et al. (2007) introduces a concept based on the Finsler metric to segment interesting fiber bundles. Most segmentation algorithms are loosely based on the concept of region-growing. Since the tensors are discrete, there is no easy way to determine how tensors change between voxels. Linear interpolation may not be a reliable method except at places with prolate profiles. A good continuous tensor approximation may be needed to ensure that shape generation is reliable (Pajevic et al., 2002). Various attempts to compute the continuous tensor are available, notable among them use the Riemannian (Pennec et al., 2006) and Log Euclidean metrics (Arsigny et al., 2006). Kindlmann et al. (2007b) use geodesic loxodromes to approximate the tensors between the voxels with a distinct advantage that the tensors are always positive definite.

To quantify and visualize the shape changes, we employ a 3D region-growing algorithm to extract the bundle surfaces. We start with initial seeds chosen from the voxels that form part of the tract. The criterion for the region-growing algorithm is chosen to be the normalized tensor scalar product (NTSP) and is mathematically described by the following equation

$$\mathrm{NTSP}(D1:D2) = \frac{D1:D2}{Trace(D1)Trace(D2)}, \quad (9)$$

$$\text{where, } D1:D2 = \sum_{j=1}^{3}\sum_{i=1}^{3}\lambda_{1i}\lambda_{2j}(e_{1i}e_{2j})^2$$

We used tri-linear interpolation NTSP to approximate the continuous tensor spread. This works best for the fiber bundles that can be delineated perfectly. The normalization of the scalar product ensures that there is no bias in the criterion due to the size of the tensor. The FA and the mode also provide constraint thresholds for restricting the region growing in high anisotropy regions. To ensure that the complete tract is extracted, multiple seeds at different spatial locations are employed to propagate the region-growing. We choose the starting voxels from within the ROIs that are used for tracking the bundles. Shape measures employ the Gaussian curvature to analyze the surface differences. Gaussian curvature is an intrinsic geometric quantity independent of the embedding and is defined as the product of the two principal curvatures k_1 and k_2 defined on the surface. Details of Gaussian curvature can be found in textbooks on differential geometry like (Carmo, 1976). Intuitively, the analysis will show that for normal subjects the Gaussian curvature will be closer to zero indicating a smoother bundle surface. A positive Gaussian curvature value denotes convex areas on the surface whereas a negative Gaussian curvature describes saddle surfaces (Fig. 7). Planar surfaces or cylindrical surfaces have Gaussian curvature $G=0$. We sample the surface points and find the curvature at each point which is subsequently analyzed for specific patterns.

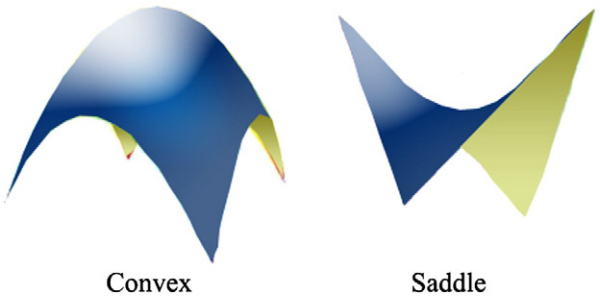

Fig. 7. Illustrations of the convex and saddle surfaces.

Experimental results

We use our brain mapping and registration framework to evaluate the hypothesis that medial temporal lobe epilepsy has associated atrophy in the fornix and cingulum fiber bundles. We conducted a population-based comparison study using 12 healthy volunteers and 15 epileptic patients. For each subject, we use high resolution anatomical MRI data as well as 25-direction DTI data. Anatomical images are conformally mapped to a solid sphere using the proposed method. The bijection inherent in the map ensures that voxels selected in the reference template are mapped back to the native space of each subject. The MRI and the DTI are affine-registered using the algorithm described in FSL (Brehens et al., 2003). To track the fibers, the seed voxels are chosen on the template. The inverse map and the corresponding affine registration parameters transform the seed voxels to the DTI space. The cingulum and the fornix fibers are illustrated in Fig. 8d. Probabilistic tracking of the bundles will generate around 2000 samples per voxel of the ROI. The anisotropy cutoff is set at 0.2 and the maximum length of the fiber path is set at 500. The following sub-sections describe the setup for ROI selection and the results of the hypothesis.

Protocol for choosing ROIs

ROI selection protocol for the cingulum and fornix bundle is explained below (Fig. 8). For the cingulum, there are 4 ROIs. The first 2 are drawn in the coronal plane at locations where the genu and the splenium of the corpus callosum intersect the mid-sagittal plane (Fig. 8a). The other 2 ROIs are drawn on the slice where the splenium intersects the mid-sagittal plane and the second one where the pons intersects the mid-sagittal plane (Fig. 8b). For the fornix bundle, 3 ROIs were drawn. The first ROI is drawn at the Foramen of Monro, the second ROI is drawn at the posterior limb of the internal capsule, and the third ROI is drawn in the coronal plane where the slice intersects the pons in the mid-sagittal plane (Fig. 8c). The ROIs were chosen carefully with expert intervention to ascertain maximum reproducibility of the fiber tracts. Only the fibers passing through these ROIs are chosen for analysis.

We had 3 raters work separately on 5 normal datasets to test the reliability of the chosen ROIs. The 3 raters performed 3 trials on each of the 5 datasets. The inter-rater and intra-rater reliability analysis was calculated and the results are presented in Table 1. Among the three raters, two raters had knowledge of the anatomy while the third rater had no particular background and was only trained to use the software. The raters manually delineated the ROIs in the DTI space with 3 trials for each dataset (Figs. 8a–c). The kappa values for the intra-rater reliability for the cingulum and the fornix were 0.94 and 0.94, respectively. The corresponding inter-rater reliability values were 0.93 and 0.94 for the cingulum and fornix, respectively.

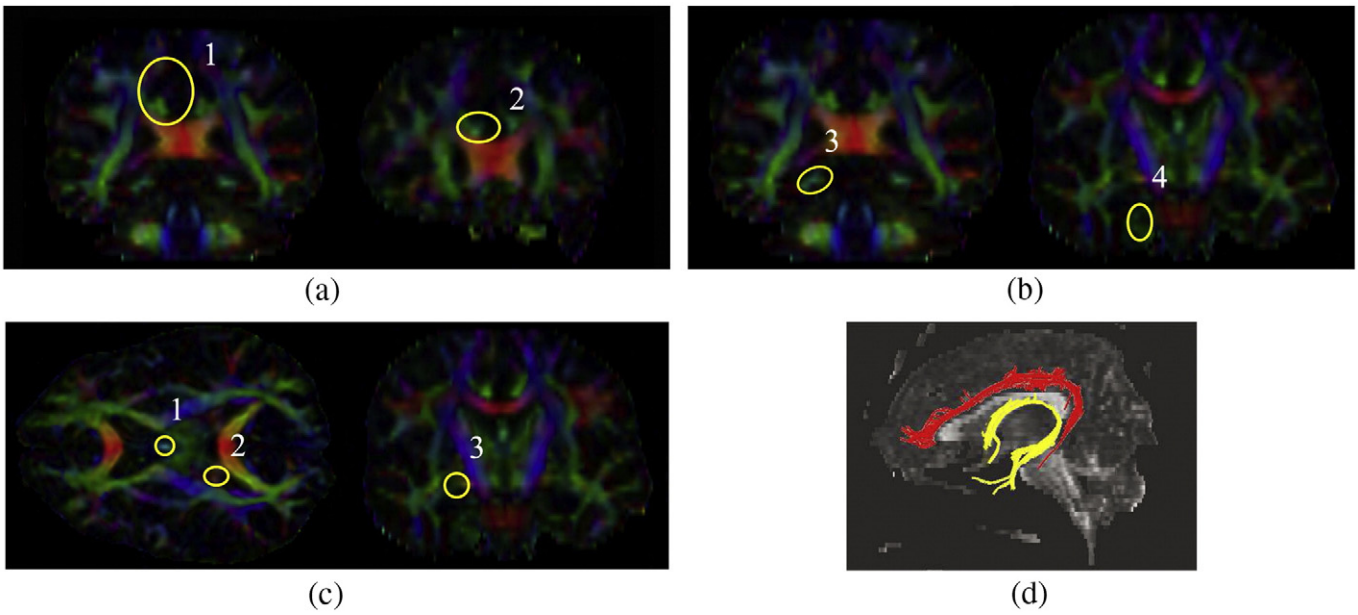

Fig. 8. (a) and (b) show the manual selection of ROIs for the cingulum in DTI. (c) shows manual selection of the ROIs for the fornix in DTI. (d) A DTI image on which the extracted cingulum and fornix fiber bundles are superimposed in red and yellow, respectively.

To test the accuracy of the mapping and registration framework, we used another reliability analysis measure called inter-modal reliability. To evaluate the inter-modal reliability, ROIs selected on the MRI template were mapped to the DTI space and used to track the fibers. The third row in Table 1 shows the kappa values for the inter-modal reliability calculated for the 5 datasets, 0.85 for the cingulum and 0.92 for the fornix. All kappa values obtained in these experiments fell in the "almost perfect" agreement range (Pantazis et al., 2010). They suggest that operator dependence is minimal and the statistical significance of the evaluation study is not affected by ROI selection protocol.

Anisotropy (volume ratio) results

The anisotropy was quantified using VR defined as the ratio of ellipsoid volume over the volume of the sphere

$$VR = 1 - \frac{27\lambda_1\lambda_2\lambda_3}{(\lambda_1+\lambda_2+\lambda_3)^3}. \quad (10)$$

It measures the ratio of the isotropic and anisotropic components at each voxel so that a lower VR value indicates more isotropy and less diffusion. We find the mean VR values of the voxels belonging to specific fiber bundles. This represents the global measure of anisotropy of the bundle. For the cingulum of the healthy volunteers, this value is around 0.187 whereas for epileptic patients, it is around 0.109. This suggest that the mean VR of the cingulum in epileptic patients is 40% less than that of the normal subjects. The fornix bundle has a normal mean VR value of 0.212 compared to the epileptic patients that have a mean VR value of 0.159, which reflects a 25% decrease. A standard t-test on the data shows that the difference between the two groups is statistically significant (p-value<0.0001). These values are consistent for the cingulum and the fornix. These results are presented in Table 2.

Shape analysis results

Fig. 9a visualizes the cingulum fiber bundle for a normal subject. The bundle surface has a smooth appearance consistent with the anatomy of the fiber. Fig. 9b shows the same fiber bundle for an epileptic patient. This bundle has a bumpy appearance, which is attributed to abnormality associated with the disease. Structural changes are clearly visualized in the surface shape. We quantify the shape variations using the Gaussian curvature. Smooth bundles are expected to have a Gaussian curvature close to zero. The region-growing algorithm uses the normalized tensor product given in Eq. (9) to create the 3D volume and the marching cubes to create the final surface. Subsequently, we calculate the Gaussian curvature at every point on the surface. The procedure is described below.

The fiber bundle is skeletonized and parameterized from 0 to t to normalize the lengths across the subjects. The Gaussian curvature is sampled along the skeleton using

$$C(r,\theta,t) = \int\int G(r,\theta,t)drd\theta dt, \quad (11)$$

where $drd\theta$ is the cross-section at the skeleton point dt and G is the Gaussian curvature at the surface point defined by r and θ. We divide Eq. (11) by the number of samples to calculate the mean Gaussian

Table 1
Average kappa values (κ) for intra-rater, inter-rater, and inter-modal reliability for 5 datasets.

Kappa values (κ)	Cingulum bundle	Fornix bundle
Intra-rater	0.94 ± 0.04	0.94 ± 0.03
Inter-rater	0.93 ± 0.04	0.94 ± 0.04
Inter-modal	0.85 ± 0.02	0.92 ± 0.04

Table 2
The mean and standard deviations of the volume ratio (VR) values of the normal subjects and the temporal lobe epilepsy patients in the cingulum (a) and the fornix (b) fiber bundles.

	Mean volume ratio ± standard deviation	p-value of t-test
Normal subjects[a]	0.187 ± 0.031	3.74 × E−06
Temporal lobe epilepsy patients[a]	0.109 ± 0.012	
Normal subjects[b]	0.212 ± 0.030	9.20 × E−05
Temporal lobe epilepsy patients[b]	0.159 ± 0.015	

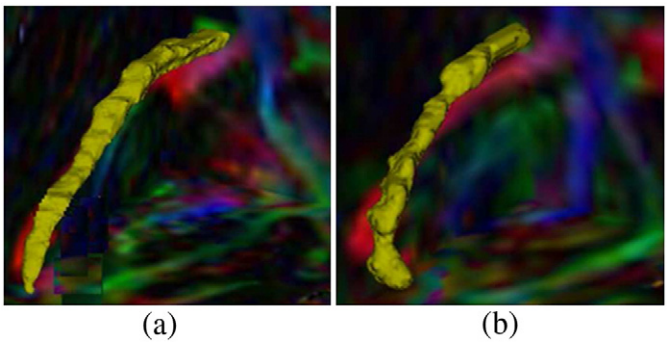

Fig. 9. Shapes of a part of cingulum fiber bundle of a normal subject (a) compared to that of an epileptic patient (b).

curvature of the bundle for a subject. Experiments conducted on 12 normal subjects and 15 epileptic patients measured the mean and standard deviation of the Gaussian curvatures for the two groups. Table 3 lists the results and shows that the epileptic patients have a positive mean Gaussian curvature indicating that they have more convex areas of high curvature. In contrast, the mean Gaussian curvature for the normal subjects is close to zero. Fig. 10 compares the histograms of the Gaussian curvatures for a normal subject and a patient. The peaks in the histograms denote smooth areas where the curvature is zero. For the normal subject, Fig. 10b, the plot goes to zero quickly on either side of the peak but for the patient, Fig. 10a, the plot goes to zero gradually indicating many areas of higher curvature. The saddle areas correspond to the left side of the peak and the convex areas correspond to the right side of the peak. The analysis results show that shape changes are successfully quantified and the differences are significant for the fiber bundles.

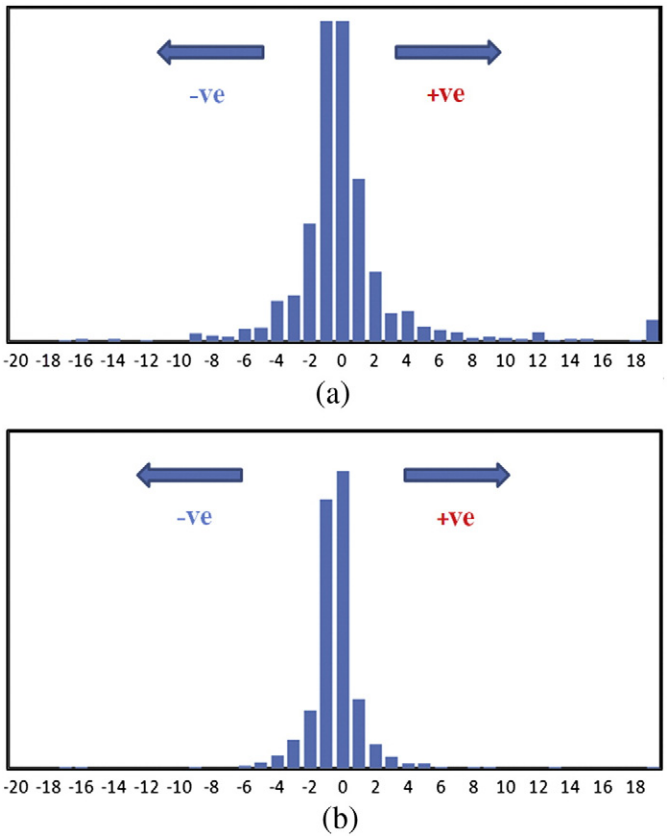

Fig. 10. Histograms of the Gaussian curvatures of the surface of the cingulum fiber bundle for a patient (a) and a normal subject (b).

Discussion

The paper presented an approach for quantitative evaluation of fiber bundles using well-known measures of anisotropy. Experiments conducted on medial temporal epilepsy subjects showed significant decreases in the anisotropy of the cingulum and the fornix fiber bundles. The abnormality was consistently reproducible by the VR measure, a quantity measuring the extent of deviation from isotropic diffusion. The discriminative power of VR was significant when compared to other anisotropic measures.

Previous DTI studies on TLE have mostly focused on specific anatomical abnormalities and used popular measures like fractional anisotropy (FA) and mean diffusivity (MD) to quantify diffusion. Most studies have reported lower FA and higher MD values for pathologies affecting hippocampi, thalamus, external capsule, corpus callosum, fornix, and cingulum (Gaolang et al., 2008, Wieshmann et al., 1999, Yoo et al., 2002, Arfanakis et al., 2002, Assaf et al., 2003). Their findings were reported on specific white matter abnormalities associated with TLE, for example, mesial temporal sclerosis or hippocampal sclerosis. Our main goal was to conduct experiments on TLE irrespective of known anatomical abnormalities and report significant differences in specific fiber tracts. The fornix and cingulum reported significant differences for the VR measure (Table 2) with a t-test significance value of $p<0.001$. FA differences were previously shown to be significant for the two bundles (Concha et al., 2005) but the experiments only targeted patients with known anatomical abnormality, i.e., TLE patients with MTS. We also quantified shape changes of the fiber bundles using differences in their surface curvature. Table 3 shows the differences in the curvature of the cingulum fiber bundle and is visualized in Fig. 9 for normal vs. an epileptic patient. Visual examination of the bundle surface confirms that atrophy is associated with a bumpy surface in the TLE patients.

Table 3
The mean and standard deviations of the Gaussian curvatures of the normal subjects and the temporal lobe epilepsy patients on the surfaces of the cingulum (a) and the fornix (b) fiber bundles.

	Mean Gaussian curvature ± standard deviation	p-value of t-test
Normal subjects[a]	0.059 ± 0.048	1.30×10^{-7}
Temporal lobe epilepsy patients[a]	0.436 ± 0.027	
Normal subjects[b]	0.043 ± 0.025	1.26×10^{-9}
Temporal lobe epilepsy patients[b]	0.478 ± 0.044	

Seed voxels for tracking of the fibers were provided by the proposed mapping framework. The motivation for the framework was to perform the analysis in the native space of the subject. This will mitigate errors associated with the spatial normalization of the DTI data which is difficult to handle due to tensor reorientation problems. The conformal parameterization of the volume was an excellent choice since it uses the intrinsic geometry of the brain for mapping. Also, since the mapping is performed on a curvature-constant domain, distortions are minimized. Moreover, the mapping is bijective and analysis can be easily transferred to the native space as desired. Mapping methods based on geometry have distinct advantages over intensity-based techniques, the latter normalizes and smoothes the data making ROI selection difficult. We used a constrained conformal mapping method using manually delineated landmarks for registration.

Landmark-based methods are generally more flexible than automatic methods since prior knowledge of the brain features can be used to drive a better alignment and registration (Pantazis et al., 2010). The landmarks were manually chosen uniformly across the brain by experts. All the structural scans were mapped to the MNI_152 template. Exact feature alignment followed by optimal shape transformation functional improved the accuracy of the mapping.

An affine registration between the MRI and the corresponding DTI completed the mapping from the MNI_152 template to each individual DTI image.

Bias in DTI analysis is attributed to artifacts due to subject motion or distortion effects during acquisition and operator dependence. The datasets were corrected for Eddy current effects using the tools available in FSL. The images were inspected after the correction and compared to the corresponding T1 image for geometrical distortion in brain regions where the ROIs would be defined. Only matched DTI and T1 scans were included in the study.

The operator can bias the ROI selection process and hence we followed a strict set of protocols for ROI selection as described in a previous section. Three raters placed the ROIs on 5 datasets to evaluate the inter-rater and intra-rater reliability which turned out to be excellent (Table 1). Moreover, ROIs defined on the MRI template and transformed to the DTI using the mapping parameters and the affine registration parameters showed good reproducibility of the fibers (inter-modal reliability).

Probabilistic tracking of fibers was the preferred choice because of its inherent ability to account for uncertainty in the tracking. To get reasonable connectivity information from the tracking, a large number of samples are generated. The generated paths represent the sampling space of the seed voxel. From the sampling space, only fiber paths that pass through these ROIs were chosen for the anisotropy analysis. Connection probabilities were not taken into consideration in this paper. Since the probabilities depend on the seed locations of the ROIs, it is unclear if changes in connectivity are significant at this time.

Finally, the surface of the fiber bundle was generated using the entire diffusion tensor information at each voxel. A simple region-growing algorithm was employed to extract the surface from the bundle volume. We used the normalized tensor scalar product as a measure of the tensor. The normalization of the tensor makes it independent of the size of the tensor and the region-growing algorithm only depends on the shape and the orientation.

To check for artifacts in the region-growing output, a sensitivity analysis was performed. We simulated fiber bundle degradation with a Gaussian disturbing function on a normal dataset. The curvature with no degradation was 0.01 which gradually increased to 0.11 for 10% degradation, 0.19 for 20% degradation, and 0.27 for 30% degradation. The sensitivity analysis confirmed that the method was sensitive to changes in the fiber bundles and thus was an excellent method to analyze the shape.

We also simulated white matter degradation by adding Gaussian white noise, $N(0;\sigma)$, where σ is the standard deviation. A normal dataset was subjected to varying levels of noise controlled by the variance σ^2 of the noise. The region-growing algorithm was executed and the fiber bundle surfaces were extracted for three noisy datasets at three different noise levels, $\sigma^2 = 10$, $\sigma^2 = 20$, and $\sigma^2 = 30$. The mean Gaussian curvatures for noise levels $\sigma^2 = 10$, $\sigma^2 = 20$, and $\sigma^2 = 30$ were calculated as 0.02, 0.03, and 0.05 respectively. The distributions of the Gaussian curvature are illustrated in Fig. 11. As noise levels increase, more convex and saddle surfaces appear as is evident from the histogram. However, the overall distribution is consistent and the mean curvature is not influenced by noise. Region growing does indeed have its disadvantages. The results of the algorithm is noisy in places where fiber mixing and fiber crossing is rampant and hence is not reliable for calculating curvature. In other words, only a well-delineated fiber tract will subsequently generate a good bundle surface for measuring curvature.

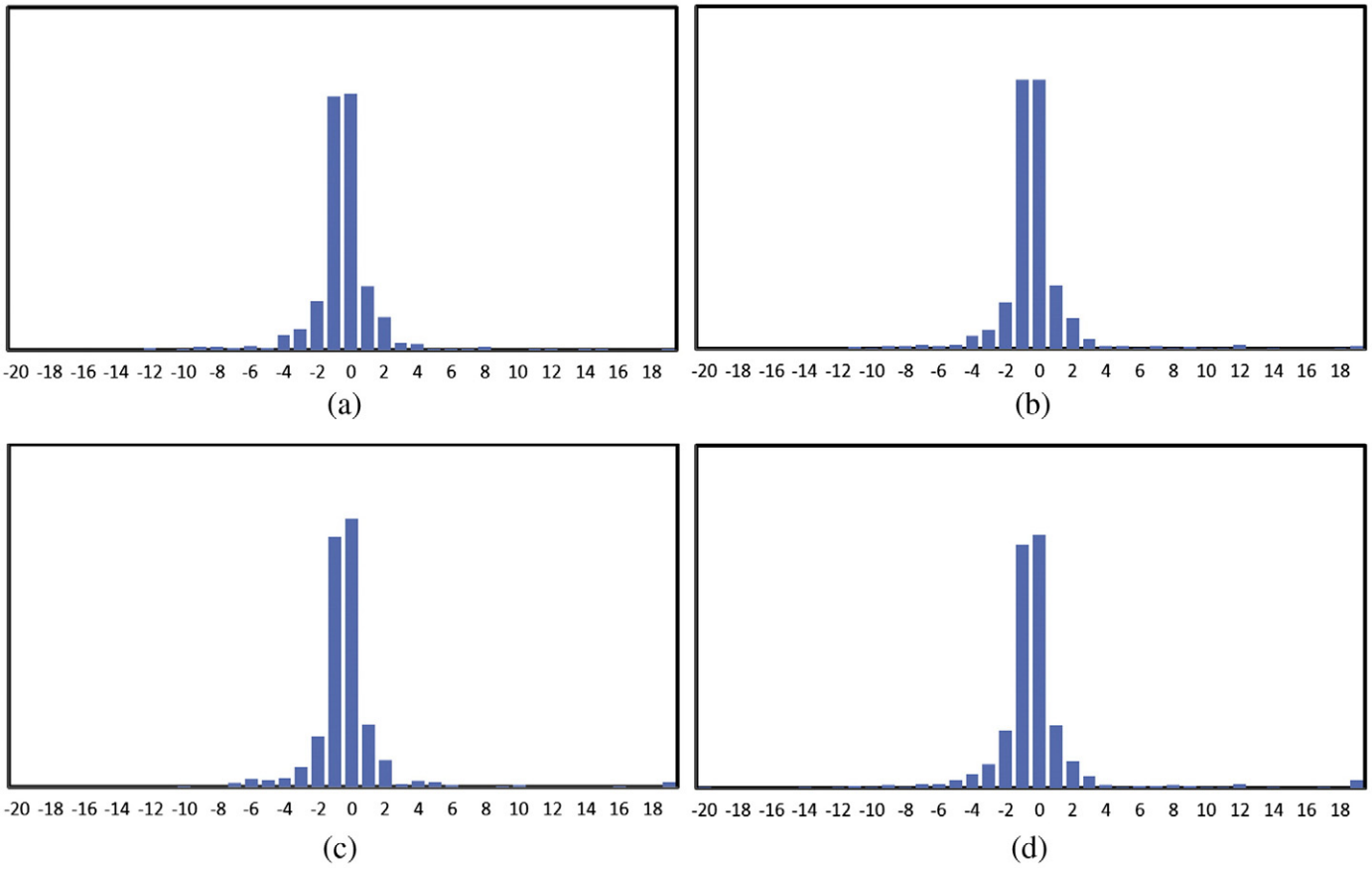

Fig. 11. (a) Curvature histogram when no noise is added. (b)–(d) Curvature histograms when noise is simulated with $\sigma^2 = 10$, $\sigma^2 = 20$, and $\sigma^2 = 30$, respectively. The histograms show some curvature values away from zero but the overall distribution is maintained.

Limitations

Limitations of the proposed framework are listed below.

1) The mean VR is the anisotropy measure that was found to be most significant for the analysis of the fornix and the cingulum fiber bundles. FA is the most popular measure for DTI studies, validated by different groups. Effectiveness of the VR is unclear and more experiments are needed to understand its significance for quantifying other areas of the white matter affected by TLE. This is an important future direction of our research.
2) Accuracy of the mapping framework is usually higher for brain regions closer to the landmarks since the registration is more accurate in these regions. Analysis of brain regions away from the landmarks needs to be evaluated or the framework should be customized to ensure accuracy in areas under study.
3) The region-growing algorithm used to generate the surface shape of the bundle may generate artifacts in areas with multi-fiber crossings and thus the measured curvature may be inaccurate. Moreover, surfaces constructed for the bundles that have low anisotropy may be noisy. Hence, region growing should be restricted to areas where the fiber tracts can be delineated reliably.

Conclusion

Based on our experiments, it is clear that for the epileptic patients, the VR provides a good discrimination for analyzing anisotropic differences in the fornix and the cingulum fiber bundles. The analysis was conducted through our brain mapping and registration framework whose accuracy was validated by a reliability study. Furthermore, we applied a region-growing algorithm based on the normalized tensor scalar product to visualize the differences in the shapes of the bundles. We observed that the mean VR decreases by 25% for the fornix and 40% for the cingulum. Moreover, the shapes are bumpy in epileptic patients whereas they are smooth in normal subjects. Quantification of the bundle shape indicates an overall positive Gaussian curvature in the epileptic patients, which is reflective of having more convex areas where atrophy due to disease is noticeable.

Conflict of interest

The authors declare that there are no conflicts of interest.

Acknowledgment

This work was supported in part by the research grants NSF IIS-0915933, NSF IIS-0937586, and NSF IIS-0713315 awarded to Jing Hua and NIH R01-EB002450 awarded to Hamid Soltanian-Zadeh.

References

Alexander, D., Pierpaoli, C., Basser, N., Gee, J., 2001. Spatial transformations of diffusion tensor magnetic resonance images. IEEE Trans. Med. Imaging 20, 1131–1139.
Arfanakis, K., Hermann, B.P., Rogers, B.P., Carew, J.D., Seidenberg, M., Meyerand, M.E., 2002. Diffusion tensor MRI in temporal lobe epilepsy. Magn. Reson. Imaging 20 (7), 511–519.
Arsigny, V., Fillard, P., Pennec, X., Ayache, N., 2006. Log-Euclidean metrics for fast and simple calculus on diffusion tensors. Magn. Reson. Med. 56 (2), 411–421.
Assaf, B.A., Mohamed, F.B., Abou-Khaled, K.J., Williams, J.M., Yazeji, M.S., Haselgrove, J., et al., 2003. Diffusion tensor imaging of the hippocampal formation in temporal lobe epilepsy. Am. J. Neuroradiol. 24 (9), 1857–1862.
Brehens, T., Woolrich, M., Jenkinson, M.R., Numes, H.J.-B., Clare, S., Matthews, P., Brady, J., Smith, S., 2003. Characterization and propagation of uncertainty in diffusion-weighted MR imaging. Magn. Reson. Med. 50 (5), 1077–1088.
Camion, V., Younes, L., 2001. Geodesic interpolating splines. Proceedings of the Third International Workshop on Energy Minimization Methods in Computer Vision and Pattern Recognition. .
Carmo, M.D., 1976. Differential Geometry of Curves and Surfaces. Prentice Hall, New York, NY, USA.
Chua, C.S., Jarvis, R., 1997. Point signatures: a new representation for 3d object recognition. Int. J. Comput. Vis. 25 (1), 63–85.
Concha, L., Beaulieu, C., Gross, D.W., 2005. Bilateral limbic diffusion abnormalities in unilateral temporal lobe epilepsy. Ann. Neurol. 57 (2), 188–196.
Drury, H., 1999. Surface-based Analyses of the Human Cerebral Cortex, Brain Warping. Elsevier, pp. 337–363.
Essen, D.V., Drury, H.A., Dickson, J., Harwell, J., Hanlon, D., Anderson, C.H., 2001. An integrated software system for surface-based analyses of cerebral cortex. J. Am. Med. Inform. Assoc. 8, 443–459.
Fischl, B., Sereno, M.I., Dale, A.M., 1999. Cortical surface-based analysis: II: Inflation, flattening, and a surface-based coordinate system. Neuroimage 9, 195–207.
Frank, L., 2001. Anisotropy in high angular resolution diffusion-weighted MRI. Magn. Reson. Med. 45, 935–939.
Friman, O., Farneback, G., Westin, C.-F., 2006. A Bayesian approach for stochastic white matter tractography. IEEE Trans. Med. Imaging 25 (8), 965–978.
Friston, K.J., Holmes, A.P., Worsley, K.J., Poline, J.-P., Frith, C.D., Frackowiak, R.S.J., 1994. Statistical parametric maps in functional imaging: a general linear approach. Hum. Brain Mapp. 2 (4), 189–210.
Gaolang, G., Concha, L., Beaulieu, C., Gross, D., 2008. Thalamic diffusion and volumetry in temporal lobe epilepsy with and without mesial temporal sclerosis. Epilepsy Res. 80, 184–193.
Gu, X., Wang, Y., Chan, T., Thompson, P., Yau, S.-T., 2004. Genus zero surface conformal mapping and its application to brain surface mapping. IEEE Trans. Med. Imaging 23 (8), 949–958.
Hagmann, P., 2004. Diffusion spectrum imaging tractography in complex cerebral white matter: an investigation of the centrum semiovale. ISMRM, p. 632.
Jones, D.K., Griffin, L.D., Alexander, D.C., Catani, M., Horsfield, M.A., Howard, R., Williams, S.C., 2002. Spatial normalization and averaging of diffusion tensor MRI data sets. Neuroimage 17 (2), 592–617.
Kazhdan, M., Funkhouser, T., Rusinkiewicz, S., 2003. Rotation invariant spherical harmonic representation of 3D shape descriptors. Symp. Geom. Process. 156–165.
Kindlmann, G., Ennis, D.B., Whitaker, R.T., Westin, C.-F., 2007a. Diffusion tensor analysis with invariant gradients and rotation tangents. IEEE Trans. Med. Imaging 26 (11), 1483–1499.
Kindlmann, G., Jos´e, S., Niethammer, M., Haker, S., Westin, C.-F., 2007b. Geodesic-loxodromes for diffusion tensor interpolation and difference measurement. pp. 1–9. URL http://dx.doi.org/10.1007/978-3-540-75757-3 1.
Melonakas, J., Kubicki, M., Niethammer, M., Miller, J., Tannenbaum, A., 2007. Locally-constrained region-based methods for DW-MRI segmentation. ICCV 1–8.
Miller, M., Banerjee, A., Christensen, G., Joshi, S., Khaneja, N., Grenander, U., Matejic, L., 1997. Statistical methods in computational neuroanatomy. Stat. Meth. Med. Res. 6 (3), 267–299.
Mori, S., Crain, B.J., Chacko, V.P., Zijl, P.C., 1999. Three-dimensional tracking of axonal projections in the brain by magnetic resonance imaging. Ann. Neurol. 45 (2), 265–269.
Muzik, O., Chugani, D., Juhasz, C., Shen, C., Chugani, H., 2000. Statistical parametric mapping: assessment of application in children. Neuroimage 12, 538–549.
Muzik, O., Chugani, D.C., Zou, G., Hua, J., Lu, Y., Lu, S., Asano, E., Chugani, H.T., 2007. Multimodality data integration in epilepsy. Int. J. Biomed. Imaging PMCID: PMC1940316.
Osada, R., Funkhouser, T., Chazzele, B., Dobkin, D., 2002. Shape distributions. Transaction Graph. 21 (4), 807–832.
Pajevic, S., Aldroubi, A., Basser, P., 2002. A continuous tensor field approximation of discrete DT-MRI data for extracting microstructural and architectural features of tissue. J. Magn. Reson. 154, 85–100.
Pantazis, D., Joshi, A., Jintao, J., Shattuck, D., Bernstein, L., Damasio, H., Leahy, R., 2010. Comparison of landmark-based and automatic methods for cortical surface registration. Neuroimage 49 (3), 2479–2493.
Park, H., Kubicki, M., Shenton, M.E., Guimond, A., McCarley, R.W., Maier, S.E., Kikinis, R., Jolesz, F.A., Westin, C.-F., 2003. Spatial normalization of diffusion tensor MRI using multiple channels. Neuroimage 20, 1995–2009.
Parker, G., 2000. Tracing fiber tracts using fast marching. Proc., Int. Soc. Magn. Reson. 8, 85.
Pennec, X., Fillard, P., Ayache, N., 2006. A reimannian framework for tensor computing. Int. J. Comput. Vis. 66, 41–66.
Schultz, T., Seidel, H.-P., 2008. Using eigenvalue derivatives for edge detection in DT-MRI data. DAGM Symposium, pp. 193–202.
Smith, S., Jenkinson, M., Johansen-Berg, H., Rueckert, D., Nichols, T., Mackay, C., Watkins, K., Ciccarelli, O., Cader, M., Matthews, P., Brehens, T., 2006. Tract-based spatial statistics: voxelwise analysis of multi-subject diffusion data. Neuroimage 31, 1487–1505.
Stejskal, E., Tanner, J., 1965. Spin diffusion measurements: spin echoes in the presence of a time-dependent field gradient. J. Chem. Phys. 42, 184–195.
Styner, M., Gerig, G., 2001. Three-dimensional medial shape representation incorporating object variability. Comput. Vis. Pattern Recognit. 2, 651–656.
Styner, M., Gerig, G., Lieberman, J., Jones, D., Weinberger, D., 2003. Statistical shape analysis of neuroanatomic structures based on medial models. Med. Image Anal. 7, 207–220.
Thompson, P., Toga, A., 2002. A framework for computational anatomy. Comput. Vis. Sci. 5, 13–34.
Thompson, P., Vidal, C., Giedd, J.N., Gochman, P., Blumenthal, J., Nicolson, R., Toga, A.W., Rapoport, J.L., 2001. Mapping adolescent brain change reveals dynamic wave of accelerated gray matter loss in very early-onset schizophrenia. Proc. Natl Acad. Sci. USA 98 (20), 11650–11655.
Vemuri, B., Mitiche, A., Aggarwal, J., 1986. Curvature-based representation of objects from range data. Image Vis. Comput. 4 (2), 107–114.
Wakana, S., Jiang, H., Nagae-Poetscher, L., Zijl, P., Mori, S., 2004. Fiber tract based atlas of human white matter anatomy. Radiology 230, 77–87.
Wang, Y., Gu, X., Chan, T.F., Thompson, P.M., Tung Yau, S., 2004. Volumetric harmonic brain mapping. IEEE Int. Symp. Biomed. Imaging 1275–1278.

Wang, Y., Lui, L., Chan, T., Thompson, P., 2005. Optimization of brain conformal mapping with landmarks. Proc. MICCAI, pp. 675–683.
Wieshmann, U.C., Clark, C.A., Symms, M.R., Barker, G.J., Birnie, K.D., Shorvon, S.D., 1999. Water diffusion in the human hippocampus in epilepsy. Magn. Reson. Imaging 17, 29–36.
Woods, R.P., Grafton, S.T., Holmes, C.J., Cherry, S.R., Mazziotta, J.C., 1998. Automated image registration: I. General methods and intrasubject, intramodality validation. J. Comput. Assist. Tomogr. 22, 139–152.
Yoo, S.Y., Chang, K.H., Song, I.C., Han, M.H., Kwon, B.J., Lee, S.H., et al., 2002. Apparent diffusion coefficient value of the hippocampus in patients with hippocampal sclerosis and in healthy volunteers. Am. J. Neuroradiol. 23 (5), 809–812.
Zhang, D., 1999. Harmonic Shape Images: a 3D Free-form Surface Representation and its Applications in Surface Matching. Ph.D. Dissertation, Robotics Institute, Carnegie Mellon University.
Zou, G., Hua, J., Gu, X., 2006. An approach for intersubject analysis of 3D brain images based on conformal geometry. Proceedings, ICIP, pp. 1193–1196.